

Theory of charge-spin conversion at oxide interfaces: The inverse spin-galvanic effect

Götz Seibold^a, Sergio Caprara^b, and Roberto Raimondi^c

^aInstitut für Theoretische Physik, BTU Cottbus-Senftenberg, PBox 101344, 03013 Cottbus, Germany

^bDipartimento di Fisica Università di Roma Sapienza, piazzale Aldo Moro 5, I-00185 Roma, Italy

^cDipartimento di Matematica e Fisica, Università Roma Tre, Via della Vasca Navale 84, 00146 Rome, Italy

ABSTRACT

We evaluate the non-equilibrium spin polarization induced by an applied electric field for a tight-binding model of electron states at oxides interfaces in LAO/STO heterostructures. By a combination of analytic and numerical approaches we investigate how the spin texture of the electron eigenstates due to the interplay of spin-orbit coupling and inversion asymmetry determines the sign of the induced spin polarization as a function of the chemical potential or band filling, both in the absence and presence of local disorder. With the latter, we find that the induced spin polarization evolves from a non monotonous behavior at zero temperature to a monotonous one at higher temperature. Our results may provide a sound framework for the interpretation of recent experiments.

Keywords: Spin-orbit coupling, spin-charge conversion, oxides interfaces

1. INTRODUCTION

It is well known that the breaking of the inversion symmetry leads to the so-called Rashba spin-orbit coupling (SOC),¹⁻³ where polar and axial vectors transform similarly.⁴ Basically this allows for two major possibilities of charge to spin conversion: The spin Hall (SH)⁵ and the inverse spin galvanic (ISG) effect,^{6,7} as well as for their Onsager reciprocal effects. While the SH effect converts an electrical current into a spin imbalance at the sample edges via an induced perpendicular spin current, the ISG effect creates a *bulk* non-equilibrium spin polarization by a flowing electrical current.^{6,8-11} The inverse SG effect corresponds then to the production of electrical current via the pumping of spin polarization.^{12,13} Both the SG^{12,13} and the ISG¹⁴⁻²⁰ effects have been observed in semiconductors. In the first case an electrical current is measured after pumping spin polarized light (SG) whereas in the second case Faraday and Kerr spectroscopies measure the spin polarization induced by the applied current. The SG effect has also been very effectively measured by spin pumping from an adjacent ferromagnet into a metallic interface,²¹ into a topological insulator surface^{23,24} and more recently into the two-dimensional electron gas (2DEG) in oxide LAO/STO heterostructures.²⁵⁻²⁸ These latter materials have emerged²⁹⁻³³ as very promising materials for the SG and ISG effect, due to the large values of the Rashba SOC parameter α as experimentally observed³⁴⁻³⁷ and also theoretically calculated,³⁸⁻⁴⁰ even though it is likely that, due to their complex band structure, the available theory⁴¹ of the SG/ISG effect developed for the 2DEG in semiconductors may not be able to capture a number of specific features. A first step in this direction has been made recently by a combination of analytical diagrammatic and numerical approaches.^{42,43}

The layout of the paper is the following. In the next section we introduce a model for the electron states relevant for describing transport at oxide LAO/STO interfaces. In section 3 we provide the necessary formalism of linear response theory for the SG and ISG effects. In section 4 we introduce an approximate effective model for electron states close to band minima. In section 5 we evaluate analytically the SG response for the effective

Further author information: (Send correspondence to Roberto Raimondi.)
Roberto Raimondi: E-mail: roberto.raimondi@uniroma3.it

model, whereas in section 6 we introduce disorder and the necessary formalism to handle it. Finally in section 7 we present a fully numerical approach which includes both cases without and with disorder. We conclude in section 8. A number of technical details are provided in the appendices.

2. THE MODEL

The electronic structure of the 2DEG at LAO/STO interfaces, perpendicular to the (001) crystal direction, is usually described^{39,44,45} within a tight-binding Hamiltonian H_0 for the Ti t_{2g} orbitals, d_{xy}, d_{xz}, d_{yz} , supplemented by local atomic spin-orbit interactions with Hamiltonian H_{aso} and an interorbital hopping with Hamiltonian H_I which is induced by the interface asymmetry.

The hopping between the d orbitals of two neighbouring cubic cells is mediated via intermediate jumps to p orbitals. For instance, the hopping between two d_{xy} orbitals along the x axis occurs via two successive hopping $d_{xy} \rightarrow p_y$ and $p_y \rightarrow d_{xy}$. In the first hop, the overlap, which is of order $\sim t_{pd}$, yields a positive sign, whereas the sign is negative $\sim -t_{pd}$ in the second one. Hence the effective $d_{xy} - d_{xy}$ hopping goes like $-t_{pd}^2/\Delta E$, with ΔE being the energy difference between d and p orbitals. As a result, in the basis $|xy\rangle, |xz\rangle, |yz\rangle$ the hopping between similar orbitals reads as

$$H_0 = \begin{pmatrix} \varepsilon_k^{xy} & 0 & 0 \\ 0 & \varepsilon_k^{xz} & 0 \\ 0 & 0 & \varepsilon_k^{yz} \end{pmatrix} \quad (1)$$

with, setting to unity the lattice spacing,

$$\begin{aligned} \varepsilon_k^{xy} &= -2t_1[\cos(k_x) + \cos(k_y) - 2] - 4t_3[\cos(k_x)\cos(k_y) - 1] \\ \varepsilon_k^{xz} &= -2(t_1 + t_3)[\cos(k_x) - 1] - 2t_2[\cos(k_y) - 1] + \Delta \\ \varepsilon_k^{yz} &= -2(t_1 + t_3)[\cos(k_y) - 1] - 2t_2[\cos(k_x) - 1] + \Delta \end{aligned}$$

where the energy difference Δ between the $|xy\rangle$ and $|xz\rangle, |yz\rangle$ states is due to the confinement of the 2DEG in the xy -plane.⁴⁶

The atomic SOC is given by

$$H_{aso} = \Delta_{aso} \begin{pmatrix} 0 & -i\tau^x & i\tau^y \\ i\tau^x & 0 & -i\tau^z \\ -i\tau^y & i\tau^z & 0 \end{pmatrix} \quad (2)$$

with τ^i denoting the Pauli matrices.

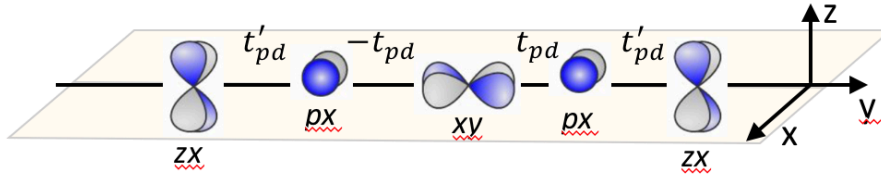


Figure 1. At the interface an orbital polarization and (or) orbital displacement results in hopping processes $\sim t'_{pd}$ as between p_x - and zx -orbitals along the y -direction. The asymmetry is visualized by a small shift of p_x -orbitals along the x -direction.

Hopping between different d orbitals may occur if inversion symmetry is broken, see Fig. 1. Consider, for instance, the two hops along the y direction, $d_{xy} \rightarrow p_x$ and $p_x \rightarrow d_{zx}$. While the first hop $\sim t_{pd}$ is as the first hop of the effective hopping between two d_{xy} orbitals discussed above, the second hop $\sim t'_{pd}$ will be forbidden in the presence of inversion symmetry. To see this consider that

$$t_{pd} = \langle p_x, \mathbf{R} + \frac{a}{2}\mathbf{y} | H | d_{xy}, \mathbf{R} \rangle,$$

where \mathbf{R} is the lattice site of the d_{xy} orbital. In the same way

$$t'_{pd} = \langle d_{zx}, \mathbf{R} + a\mathbf{y} | H | p_x, \mathbf{R} + \frac{a}{2}\mathbf{y} \rangle.$$

In both cases, H is the full Hamiltonian. If H is invariant with respect to the inversion $z \rightarrow -z$, then necessarily $t'_{pd} = 0$, because p_x is even, while d_{zx} is odd. Clearly if H has terms which are not invariant for $z \rightarrow -z$, then $t'_{pd} \neq 0$. As a result the interface asymmetry hopping reads⁴⁴

$$H_I = \gamma \begin{pmatrix} 0 & -2i \sin(k_y) & -2i \sin(k_x) \\ 2i \sin(k_y) & 0 & 0 \\ 2i \sin(k_x) & 0 & 0 \end{pmatrix}. \quad (3)$$

In the following we use the parameters, $t_1 = 0.277$ eV, $t_2 = 0.031$ eV, $t_3 = 0.076$ eV, $\Delta = 0.4$ eV, $\Delta_{aso} = 0.010$ eV, $\gamma = 0.02$ eV, which have been derived in Ref.³⁹ from projecting DFT on the t_{2g} Wannier states. Note that for the splitting Δ we take a value intermediate between the theoretical ($\Delta = 0.19$ eV) and the experimental one ($\Delta = 0.6$ eV). The left panel of Fig. 2 shows the band dispersions along the x axis for these values of the parameters. The bands come naturally in three pairs, which are split by the combined effect of the spin-orbit coupling and the inversion symmetry breaking. For our analysis we have selected three different values of the chemical potential for corresponding filling regimes. For $\mu = 0.3$ eV, only the lowest pair of bands (1,2) is occupied. The chemical potential $\mu = 0.425$ eV is close to the Lifshitz point, where the spin-orbit splitting is large and the pairs of bands (3,4) and (5,6) start to be filled. Finally, the chemical potential $\mu = 0.7$ eV is in the regime, where all pairs of bands (1,2), (3,4) and (5,6) are occupied.

We now analyze the chirality for each eigenstate band $p = 1, \dots, 6$ by computing the spin at each momentum point of the Fermi surface (FS) according to

$$S^\alpha(p, k_F) = \sum_{n, \sigma, \sigma'} \Phi_{n, \sigma}^*(p, k_F) \tau_{\sigma, \sigma'}^\alpha \Phi_{n, \sigma'}(p, k_F)$$

where $\Phi_{n, \sigma'}(p, k_F)$ are the eigenfunctions of the system at momentum k_F . The indices $n = xy, xz, yz$ and σ label the orbital and its spin. Then the chirality of the p -th band can be obtained from

$$\alpha(p) = \arcsin \left(\frac{\mathbf{k}_F \times \mathbf{S}(p, k_F) \cdot \mathbf{e}_z}{|\mathbf{k}_F| |\mathbf{S}(p, k_F)|} \right).$$

Fig. 2 shows the chiralities for each pair of bands at selected chemical potentials and the corresponding FSs. For the lowest pair of bands (1,2) the momentum dependent spin pattern displays a vortex-type structure with the core centered at $\Gamma = (0, 0)$. Thus, even when the FS changes from electron- to hole-like between $\mu = 0.5$ and $\mu = 0.6$, the corresponding chiralities are always confined to $\alpha(p) \approx \pm\pi/2$ without any sign change in α . For the middle pair of bands (3,4) the spin structure is composed of two vortex patterns (with the same vorticity) centered at $(\pi, 0)$ and $(0, \pi)$. As a consequence, the spin texture vanishes along the diagonals and a Rashba-type description along this direction fails. In section 4 we will come back to this point. However, for small μ and all other momenta the chirality also starts at $\alpha \approx \pm\pi/2$ but then on average becomes smaller with increasing chemical potential and eventually changes sign for $\mu \approx 1.5$. An analogous situation occurs for the uppermost pair of bands where the 'spin-vortex core' is centered at (π, π) . In this case the chiralities also change sign upon increasing the chemical potential while at small μ one again recovers $\alpha \approx \pm\pi/2$.

3. LINEAR RESPONSE THEORY

In this paper we aim at evaluating the spin polarization induced by an externally applied electric field. To be definite we take the electric field along the x axis and the spin polarization along the y axis. To linear order in the applied field we write the spin polarization as

$$s^y(\omega) = \sigma^{ISG}(\omega) E_x(\omega), \quad (4)$$

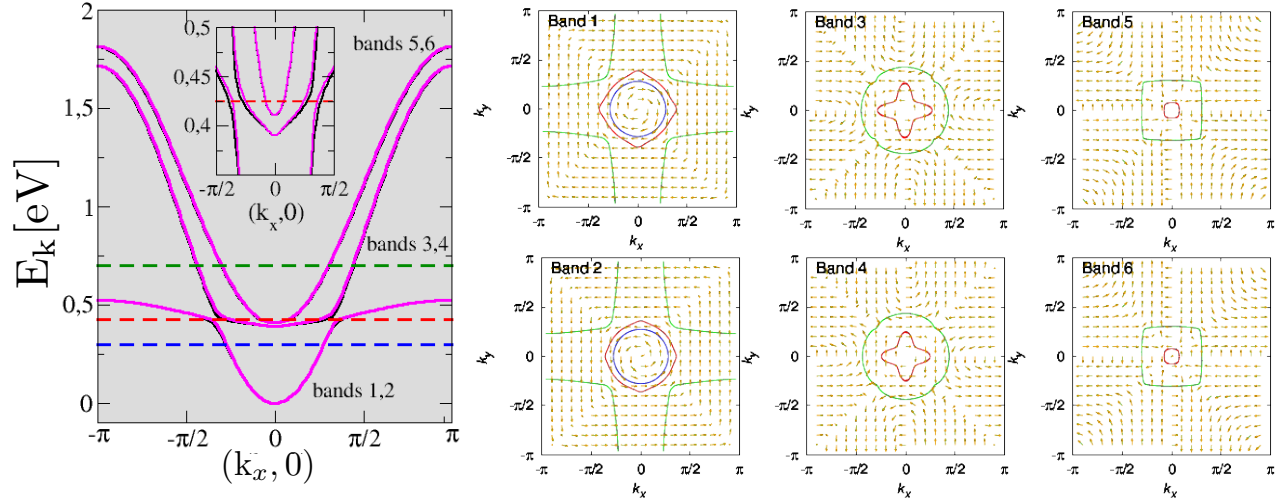


Figure 2. Left panel: Structure of the t_{2g} interface bands. The inset enlarges the region around the 'Lifshitz' point where the spin-orbit splitting is large. The horizontal dashed lines in the main panel refer to three values of chemical potential: $\mu = 0.3$ eV (blue line), $\mu = 0.425$ eV (red line) and $\mu = 0.7$ eV (green line). The right panel displays the spin texture for the three pairs of bands together with their Fermi surfaces. For the lower pair of bands (1,2) the spins point in the opposite direction.

where σ^{ISG} , the ‘‘conductivity’’ for the ISG effect, can be obtained by the zero-momentum limit of the Fourier transform $R_{yx}(\omega)$ of the response function (henceforth the symbols in capital letters indicate the operators for spin density and charge current) defined as

$$R_{yx}(t, \mathbf{r}) = -i\theta(t) \langle [S^y(t, \mathbf{r}), J_x] \rangle, \quad (5)$$

where the brackets stand for the quantum-statistical average and $\theta(t)$ is the Heaviside step function. The frequency-dependent ISG conductivity reads

$$\sigma^{ISG}(\omega) = \lim_{\eta \rightarrow 0^+} \Re \left[\frac{R_{yx}(\omega)}{i(\omega + i\eta)} \right] = -\pi\delta(\omega)R'_{yx}(0) + \mathcal{P} \frac{R''_{yx}(\omega)}{\omega} \equiv D^{ISG}\delta(\omega) + \mathcal{P} \frac{R''_{yx}(\omega)}{\omega}, \quad (6)$$

where the first term will be referred to as the Drude singular term and the second as the regular term, in analogy with the terminology used in the case of the optical conductivity. Because under time reversal both the charge current and the spin polarization are odd, according to the Onsager relation, the SG and ISG conductivities are equal.⁴¹ For this reason we will use the term SG conductivity (SGC) for both direct and inverse effects. The calligraphic symbol \mathcal{P} stands for the principal part. The real $R'_{yx}(\omega)$ and the imaginary $R''_{yx}(\omega)$ parts of the response function are related by the Kramers-Kronig relation (KKR)

$$R'_{yx}(\omega) = \frac{1}{\pi} \int_{-\infty}^{\infty} d\omega' \frac{R''_{yx}(\omega')}{\omega' - \omega}. \quad (7)$$

By integration over the frequency, thanks to the KKR, the SGC satisfies the following sum rule

$$\int_{-\infty}^{\infty} d\omega \sigma^{ISG}(\omega) = 0 \quad (8)$$

due to the fact that for the SGC there is no ‘diamagnetic’ contribution as opposed to the optical conductivity.

In the following we are going to apply the above formulae to the model introduced in section 2. To this end, it is instructive to consider first the case of the Rashba SOC for a 2DEG with quadratic dispersion relation in

the effective mass approximation. The insight gained in this simpler case will guide us also in the analysis of the model with a complex band structure. We consider then the Rashba-Bychkov Hamiltonian³

$$H = \frac{p^2}{2m} + \alpha(\tau^x p_y - \tau^y p_x), \quad (9)$$

where m is the effective mass and α the SOC. The 2DEG is confined to the xy plane and p_x and p_y are the momentum operators along the two coordinate axes. Clearly there are two eigenvalues $E_{\pm}(p) = p^2/2m \pm \alpha p$ with the corresponding eigenstates of (9) being plane waves whose spin quantization axis is fixed by the momentum direction

$$|\mathbf{p}, s\rangle = \frac{1}{\sqrt{2}} \begin{pmatrix} s \tau e^{-i\theta} \\ 1 \end{pmatrix}, \quad s = \pm 1 \quad (10)$$

where $\tan(\theta) = p_y/p_x$. The ISG response function at finite frequency and momentum reads

$$R_{yx}(\omega, \mathbf{q}) = \sum_{\mathbf{p}, s_1, s_2} \langle \mathbf{p}, s_1 | S^y | \mathbf{p}, s_2 \rangle \langle \mathbf{p}, s_2 | J_x | \mathbf{p}, s_1 \rangle \frac{f(E_{s_1}(\mathbf{p}) - \mu) - f(E_{s_2}(\mathbf{p} + \mathbf{q}) - \mu)}{\omega + i\eta + E_{s_1}(\mathbf{p}) - E_{s_2}(\mathbf{p} + \mathbf{q})}, \quad (11)$$

where $f(E)$ is the Fermi distribution function at temperature T . Depending on the values of the spin indices, one has intraband ($s_1 = s_2 = \pm 1$) and interband ($s_1 = -s_2 = \pm 1$) contributions. In the dynamic limit, when the momentum goes to zero at finite frequency, the intraband contribution vanishes. For the model of Eq.(9) the interband matrix elements for spin density $S^y = \tau^y/2$ and charge current $J_x = (-e)(p_x/m - \alpha\tau^y)$ read

$$\begin{aligned} \langle \mathbf{p}, s | S^y | \mathbf{p}, -s \rangle &= \frac{1}{2}(-is) \sin(\theta), \\ \langle \mathbf{p}, -s | J_x | \mathbf{p}, s \rangle &= (-e)\alpha(is) \sin(\theta), \end{aligned}$$

and the zero-momentum response function becomes

$$R_{yx}(\omega) = \frac{1}{2}(-e)\alpha \sum_{\mathbf{p}s} \sin^2(\theta) \frac{f(E_s(\mathbf{p}) - \mu) - f(E_{-s}(\mathbf{p}) - \mu)}{\omega + i\eta + E_s(\mathbf{p}) - E_{-s}(\mathbf{p})}. \quad (12)$$

At zero temperature, there are two FSs corresponding to the two spin helicity bands with Fermi momenta $p_{\pm} = \sqrt{2m\mu + (m\alpha)^2} \mp m\alpha$. The evaluation of the imaginary part of the zero-momentum response function leads to ($\eta \rightarrow 0^+$)

$$R''_{yx}(\omega) = \frac{e}{32\alpha} \omega [\theta(|\omega| - 2\alpha p_+) - \theta(|\omega| - 2\alpha p_-)], \quad (13)$$

showing an antisymmetric behavior with respect to the frequency ω . The spectral weight, at positive frequency, is confined in the range $2\alpha p_+ < \omega < 2\alpha p_-$. The two frequencies delimiting the interval are nothing but the spin-orbit splitting at the two Fermi surfaces. We note, and this will turn out useful when discussing the numerical calculations, that at finite η , the imaginary part remains finite and acquires a linear-in-frequency behavior around the origin, whose slope vanishes as η . The Drude weight, according to Eq. (6) can be easily obtained by the KKR relation (7) to read

$$D^{ISG} = -\frac{\pi}{2} e N_0 \alpha, \quad (14)$$

where $N_0 = m/(2\pi)$ is the single-particle density of states of the 2DEG. For the sake of simplicity we have chosen units such $\hbar = 1$. There are two features worth noticing. The first is that the Drude weight is controlled by the sign of the SOC. The second is that the Drude weight arises from the interband transitions between the spin-orbit split bands. This must be compared with the case of optical conductivity for the electron gas, where the Drude weight arises from the diamagnetic contribution to the current. In the present case, due to the sum

rule (8), the Drude low-frequency peak yields information about the spectral weight of interband transitions at finite frequency. To the best of our knowledge this feature has not been noticed before.

In the following of the paper we will consider the effect of disorder, but it is instructive to make here an heuristic discussion. In the presence of spin-independent disorder, due to the form (10) of the eigenstates, the electron spin acquires a finite relaxation rate τ_s^{-1} . This mechanism, which is known as the Dyakonov-Perel relaxation, arises because, at each scattering event, the change in momentum also affects the spin eigenstate. As a result, in the diffusive approximation, $\omega\tau \ll 1$, the spin density obeys a Bloch equation⁵¹

$$\frac{ds^y}{dt} = -\frac{1}{\tau_s}(s^y - s_0), \quad (15)$$

where $s_0 = -e\alpha N_0\tau E$ represents the steady-state nonequilibrium spin polarization⁸ induced by an applied electric field E along the x axis and τ is the momentum relaxation scattering time (not to be confused with the Pauli matrices τ^i). According to Ref.⁵¹ the Dyakonov-Perel relaxation rate reads

$$\frac{1}{\tau_s} = \frac{1}{2\tau} \frac{4\alpha^2 p_F^2 \tau^2}{1 + 4\alpha^2 p_F^2 \tau^2}. \quad (16)$$

By Fourier transforming (15) to frequency ω , one obtains the SGC in the form

$$\sigma^{ISG}(\omega) = -e\alpha N_0 \frac{\tau}{\tau_s} \frac{\tau_s^{-1}}{\omega^2 + \tau_s^{-2}}, \quad (17)$$

which has a Lorentzian lineshape and evolves to a singular contribution in the weak scattering limit $\tau \rightarrow \infty$. More precisely by integrating over frequency one obtains

$$\int_{-\infty}^{\infty} d\omega \sigma^{ISG}(\omega) = -e\alpha N_0 \pi \frac{\tau}{\tau_s} = -\frac{\pi}{2} e\alpha N_0, \quad (18)$$

which reproduces the Drude weight of Eq. (14). Notice that in the last step we made use of the fact that the spin relaxation time becomes twice the momentum relaxation time in the weak scattering limit according to Eq. (16). Eq. (18) seems to violate the sum rule (8), but this is not the case. The form (17) for the SGC has been derived in the diffusive approximation, which is valid for frequencies $\omega \ll \tau^{-1}$ well below the region of the interband spectral weight. Hence, the form (17) captures only the low frequency spectral weight, which evolves in the singular Drude weight in the limit of vanishing disorder. The effect of disorder is then to eliminate the Drude singular contribution and to yield a finite SGC at zero frequency, which is the result of a finite slope of the imaginary part of the response function. The microscopic approach in the presence of disorder is discussed in section 6 and details about the frequency dependence are developed in the appendix B.

4. EFFECTIVE MODELS

Around the Γ point the non-interacting part of the Hamiltonian (1) reads

$$\varepsilon_k^{xy} = (t_1 + 2t_3)k^2 \quad (19)$$

$$\varepsilon_k^{xz} = (t_1 + t_3)k_x^2 + t_2 k_y^2 + \Delta \quad (20)$$

$$\varepsilon_k^{yz} = (t_1 + t_3)k_y^2 + t_2 k_x^2 + \Delta, \quad (21)$$

where $k^2 = k_x^2 + k_y^2$. The atomic SOC [$\sim \tau^z$, cf. Eq. (2)] lifts the degeneracy between xz and yz but leaves the spin degeneracy, cf. Fig. 3. One obtains the new $-(+)$, corresponding to the pairs of bands (3,4) and (5,6) respectively,

$$E_\sigma^\pm = \Delta + \frac{1}{2}(t_1 + t_2 + t_3)k^2 \pm \frac{1}{2}\sqrt{(t_1 + t_3 - t_2)^2(k_x^2 - k_y^2)^2 + 4\Delta_{aso}^2}$$

and eigenfunctions

$$|xz, \uparrow\rangle = ia|+, \uparrow\rangle + ib|-, \uparrow\rangle \quad (22)$$

$$|yz, \uparrow\rangle = -b|+, \uparrow\rangle + a|-, \uparrow\rangle \quad (23)$$

$$|xz, \downarrow\rangle = ia|+, \downarrow\rangle + ib|-, \downarrow\rangle \quad (24)$$

$$|yz, \downarrow\rangle = b|+, \downarrow\rangle - a|-, \downarrow\rangle \quad (25)$$

with

$$a \approx \frac{1}{\sqrt{2}} \sqrt{1 + \frac{\varepsilon^{xz} - \varepsilon^{yz}}{(\varepsilon^{xz} - \varepsilon^{yz})^2 + 4\Delta_{aso}^2}} \approx \frac{1}{\sqrt{2}} \left(1 + \frac{1}{4\Delta_{aso}} (t_1 + t_3 - t_2)(k_x^2 - k_y^2) \right), \quad b = \sqrt{1 - a^2}$$

In the basis $|+, \uparrow\rangle, |+, \downarrow\rangle, |-, \uparrow\rangle, |-, \downarrow\rangle$ the asymmetry hopping is given by

$$\begin{aligned} H_I &= \sqrt{2}\gamma(k_y + ik_x)|xy, \uparrow\rangle\langle+, \uparrow| + h.c. \\ &+ \sqrt{2}\gamma(k_y - ik_x)|xy, \downarrow\rangle\langle+, \downarrow| + h.c. \\ &+ \sqrt{2}\gamma(k_y - ik_x)|xy, \uparrow\rangle\langle-, \uparrow| + h.c. \\ &+ \sqrt{2}\gamma(k_y + ik_x)|xy, \downarrow\rangle\langle-, \downarrow| + h.c. \end{aligned}$$

and the residual coupling of H_{aso} with the xy -level reads

$$\begin{aligned} H_{aso} &= \sqrt{2}\Delta_{aso}|xy, \uparrow\rangle\langle+, \downarrow| + h.c. \\ &+ \sqrt{2}\Delta_{aso}|xy, \downarrow\rangle\langle+, \uparrow| + h.c. \\ &- \frac{1}{2\sqrt{2}}(t_1 + t_3 - t_2)(k_x^2 - k_y^2)|xy, \uparrow\rangle\langle-, \downarrow| + h.c. \\ &- \frac{1}{2\sqrt{2}}(t_1 + t_3 - t_2)(k_x^2 - k_y^2)|xy, \downarrow\rangle\langle-, \uparrow| + h.c. \end{aligned}$$

In the following we restrict to the region close to the Γ point, where $\Delta_{aso} > tk^2$, and neglect therefore the two latter terms in H_{aso} resulting in the effective coupling structure depicted in panel (b) of Fig. 3. We can now calculate the effective interactions between levels α, β in 2nd order perturbation theory

$$\langle\alpha|H^{(2)}|\beta\rangle = -\frac{1}{2} \sum_n \left(\frac{1}{E_n - E_\alpha} + \frac{1}{E_n - E_\beta} \right) H_{\alpha,n} H_{n,\beta} \quad (26)$$

and α, β either corresponds to the xy or to the \pm levels. For the xy states one finds

$$\begin{aligned} \langle xy, \uparrow | H^{(2)} | xy, \downarrow \rangle &\approx - \frac{\langle xy, \uparrow | H_I | +, \uparrow \rangle \langle +, \uparrow | H_{aso} | xy, \downarrow \rangle}{\Delta} \\ &- \frac{\langle xy, \uparrow | H_{aso} | +, \downarrow \rangle \langle +, \downarrow | H_I | xy, \downarrow \rangle}{\Delta} \end{aligned}$$

and similarly for $\langle xy, \downarrow | H^2 | xy, \uparrow \rangle$. Inserting the matrix elements yields an effective *Rashba* SOC $\sim k_y \tau^x - k_x \tau^y$

$$H_{xy}^{SOC} = -4 \frac{\gamma \Delta_{aso}}{\Delta} \begin{pmatrix} 0 & k_y + ik_x \\ k_y - ik_x & 0 \end{pmatrix} = -\alpha_{xy} (\tau^x k_y - \tau^y k_x) \quad (27)$$

with a *negative* coupling constant with $\alpha_{xy} = 4\gamma\Delta_{aso}/\Delta$.

From Fig. 3 one can see that the same matrix elements also mediate the 2nd order interaction between the $+, \sigma$ and $+, -\sigma$ states. Since in this case the denominator in Eq. (26) is negative we obtain a *positive* coupling $\alpha_+ = 4\gamma\Delta_{aso}/\Delta$ for the E^+ states

$$H_{E^+}^{SOC} = 4 \frac{\gamma \Delta_{aso}}{\Delta} \begin{pmatrix} 0 & k_y - ik_x \\ k_y + ik_x & 0 \end{pmatrix} = \alpha_+ (\tau^x k_y + \tau^y k_x). \quad (28)$$

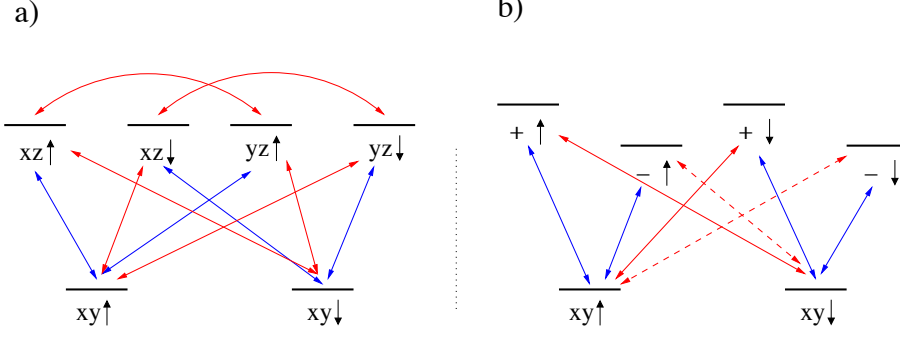


Figure 3. Level structure and interactions of the three-band Hamiltonian. Interactions of $H_{aso} \sim \Delta_{aso}$ Eq. (2) are shown in red and those of the asymmetry hopping H_I Eq. (3) are indicated in blue. The red dashed lines correspond to a atomic SO interaction which around the Γ -point (i.e. $\sim tk^2 < \Delta_{aso}$) is much smaller than the matrix elements represented by the solid lines. Panel (a) corresponds to the original Hamiltonian whereas in (b) the atomic SOC between xz and yz has been diagonalized.

Moreover the off-diagonal matrix elements in Eq. (28) are c.c. to those of Eq. (27) which means that the $+, \sigma$ and $+, -\sigma$ states are interacting via a *Dresselhaus* coupling $\sim k_y \tau^x + k_x \tau^y$.

The effective interactions between $-, \sigma$ and $-, -\sigma$ can be again obtained from 2nd order perturbation theory in the limit $tk^2 < \Delta_{aso}$ which now involves the matrix elements represented by the dashed lines in Fig. 3. The resulting effective coupling reads

$$H_-^{SOC} = -\frac{\gamma(t_1 + t_3 - t_2)(k_x^2 - k_y^2)}{\Delta} \begin{pmatrix} 0 & k_y + ik_x \\ k_y - ik_x & 0 \end{pmatrix} = -\beta(k_x^2 - k_y^2)(\tau^x k_y - \tau^y k_x) \quad (29)$$

and therefore corresponds to a linear Rashba SOC but with a coupling constant $\sim (k_x^2 - k_y^2)$.

5. THE CLEAN LIMIT

In this section we evaluate the Drude weight for the effective models discussed in section 4.

5.1 xy bands

In this case the eigenvalues and eigenvectors corresponding to the Hamiltonian (27) read

$$E_{\pm}^{xy} = \frac{k^2}{2m} \pm \alpha_{xy} k, \quad |\pm\rangle = \frac{1}{\sqrt{2}} \begin{pmatrix} \mp i e^{-i\theta} \\ 1 \end{pmatrix} \quad (30)$$

with $\hat{p}_x = \cos(\theta)$ and $\hat{p}_y = \sin(\theta)$. As for the Rashba model (9), the spin operator is simply the Pauli matrix $S^y = \tau^y/2$ and the charge current is similar to the 2DEG case $J_x = (-e)(k_x/m\tau^0 + \alpha_{xy}\tau^y)$. The interband matrix elements read

$$\langle \mathbf{k}, s | S^y | \mathbf{k}, -s \rangle = \frac{1}{2} i s \sin(\theta), \quad \langle \mathbf{k}, -s | J_x | \mathbf{k}, s \rangle = -i s \sin(\theta) (-e) \alpha_{xy}$$

and the response function (in the zero-temperature limit) gives

$$R'_{yx}(\omega \rightarrow 0) = \frac{1}{2} (-e) \alpha_{xy} \sum_{\mathbf{p}s} \sin^2(\theta) \frac{\theta(E_s^{xy}(\mathbf{p}) - \mu) - \theta(E_{-s}^{xy}(\mathbf{p}) - \mu)}{E_s^{xy}(\mathbf{p}) - E_{-s}^{xy}(\mathbf{p})} = \frac{1}{2} (-e) \alpha_{xy} N_0,$$

which leads to the Drude weight

$$D_{xy}^{ISG} = \frac{\pi}{2} e \alpha_{xy} N_0 \quad (31)$$

with an opposite sign as compared to the 2DEG case of Eq. (14).

5.2 E^- bands

In this case the eigenvalues and eigenvectors corresponding to the Hamiltonian (29) read

$$E_{\pm}^- = \frac{k^2}{2m} \pm \beta|\zeta|k^3, \quad |\pm\rangle = \frac{1}{\sqrt{2}} \begin{pmatrix} \mp i \frac{\zeta}{|\zeta|} e^{-i\theta} \\ 1 \end{pmatrix} \quad (32)$$

where $\zeta = \hat{k}_x^2 - \hat{k}_y^2$ with $\hat{k}_x = \cos(\theta)$ and $\hat{k}_y = \sin(\theta)$. In this case the spin operator reads $S^y = -\gamma(k_x^2 - k_y^2)\tau^y/2$, while the charge current has a more complicated structure as compared to the 2DEG case $J_x = (-e) \left(\frac{k_x}{m} \tau^0 - 2\beta k_x k_y \tau^x + \beta(3k_x^2 - k_y^2)\tau^y \right)$. The interband matrix elements read

$$\begin{aligned} \langle \mathbf{k}, s | \tau^y | \mathbf{k}, -s \rangle &= \imath s \frac{\zeta}{|\zeta|} \sin(\theta) \\ \langle \mathbf{k}, -s | \tau^y | \mathbf{k}, s \rangle &= -\imath s \frac{\zeta}{|\zeta|} \sin(\theta) \\ \langle \mathbf{k}, s | \tau^x | \mathbf{k}, -s \rangle &= \imath s \frac{\zeta}{|\zeta|} \cos(\theta) \\ \langle \mathbf{k}, -s | \tau^x | \mathbf{k}, s \rangle &= -\imath s \frac{\zeta}{|\zeta|} \cos(\theta). \end{aligned}$$

In the response function

$$\begin{aligned} R'_{xy}(0) &= -(-e) \sum_{\mathbf{k}, s} \frac{1}{2} (-\gamma k^2) (\hat{k}_x^2 - \hat{k}_y^2) k^2 \left[-2\beta \hat{k}_x^2 \hat{k}_y^2 + \beta(3\hat{k}_x^2 \hat{k}_y^2 - \hat{k}_y^4) \right] \frac{\theta(\mu - E_s^-(\mathbf{k})) - \theta(\mu - E_{-s}^-(\mathbf{k}))}{2s\beta|\zeta|k^3} \\ &= (-e) \frac{\gamma}{2} \int_0^{2\pi} \frac{d\theta}{2\pi} (\hat{k}_x^2 - \hat{k}_y^2)^2 \frac{\hat{k}_y^2}{|\zeta|} \int_{k_-}^{k_+} \frac{dk}{2\pi} k^2 \\ &= (-e) \frac{\gamma}{2} \int_0^{2\pi} \frac{d\theta}{2\pi} (\hat{k}_x^2 - \hat{k}_y^2)^2 \frac{\hat{k}_y^2}{|\zeta|} \frac{k_+^3 - k_-^3}{6\pi} \\ &= (-e) \gamma k_F^2 \beta k_F^2 N_0 \left(-\frac{1}{4} \right) \end{aligned}$$

the factors ζ disappear and the Drude weight reads

$$D_-^{ISG} = (-e) \left(\frac{\pi}{4} \gamma p_F^2 \beta p_F^2 N_0 \right). \quad (33)$$

5.3 E^+ bands

In this case the eigenvalues and eigenvectors corresponding to the Hamiltonian (28) read

$$E_{\pm}^{xy} = \frac{k^2}{2m} \pm \alpha_+ k, \quad |\pm\rangle = \frac{1}{\sqrt{2}} \begin{pmatrix} \mp i e^{i\theta} \\ 1 \end{pmatrix} \quad (34)$$

with $\hat{k}_x = \cos(\theta)$ and $\hat{k}_y = \sin(\theta)$. In this case the spin operator reads $S^y = \gamma(k_x^2 - k_y^2)\tau^y/2$, while the charge current is $J_x = (-e) \left(\frac{p_x}{m} \tau^0 + \alpha_+ \tau^y \right)$. The interband matrix elements are

$$\begin{aligned} \langle \mathbf{k}, s | \tau^y | \mathbf{k}, -s \rangle &= -\imath s \sin(\theta), \\ \langle \mathbf{k}, -s | \tau^y | \mathbf{k}, s \rangle &= \imath s \sin(\theta). \end{aligned}$$

The response function is

$$\begin{aligned}
R'_{xy}(0) &= -(-e)\gamma \sum_{\mathbf{k},s} k^2 (\hat{k}_x^2 - \hat{k}_y^2) \hat{k}_y^2 \frac{\alpha_+}{2} \frac{\theta(\mu - E_s^+(\mathbf{k})) - \theta(\mu - E_{-s}^+(\mathbf{k}))}{2s\alpha_+k} \\
&= -(-e)\frac{\gamma}{2} \int_0^{2\pi} \frac{d\theta}{2\pi} (\hat{k}_x^2 - \hat{k}_y^2) \hat{k}_y^2 \int_{k_-}^{k_+} \frac{k^2 dk}{2\pi} \\
&= (-e)\gamma k_F^2 \alpha_+ N_0 \left(-\frac{1}{4}\right)
\end{aligned}$$

and the Drude weight is

$$D_+^{ISG} = (-e) \left(\frac{\pi}{4} \gamma p_F^2 \alpha_+ N_0\right). \quad (35)$$

6. THE DISORDERED LIMIT

It is well known that in the presence of disorder, the Drude weight in the formula for the optical conductivity is suppressed and the spectral weight goes into the regular part. In the Drude model, the regular part, as function of the frequency, has a Lorentzian shape whose width is controlled by the scattering rate τ^{-1} (not to be confused with the Pauli matrices). Such a transfer of spectral weight from the singular to the regular part occurs also in the case of the SGC. To this end we need to introduce disorder in our model. This will be done in the numerical computation of the next section, whereas in this section we introduce disorder within the effective models derived in section 4 by using the standard diagrammatic impurity technique. This technique has been applied to the Rashba model for the evaluation of the ISG effect,⁸ anisotropy magnetoresistance^{47,50} and spin Hall effect.⁴⁸ We review here the basic aspects by focusing on the case of the xy-bands, which is equivalent to the Bychkov-Rashba model in the 2DEG. By following the standard procedure, disorder is introduced as a random potential $V(\mathbf{r})$, with zero average $\langle V(\mathbf{r}) \rangle = 0$ and white-noise correlations $\langle V(\mathbf{r})V(\mathbf{r}') \rangle = n_i u^2 \delta(\mathbf{r} - \mathbf{r}')$, with n_i being the impurity concentration. By Fermi golden rule, one associates a scattering rate $\tau^{-1} = 2\pi n_i u^2 N_0$, where N_0 is the single-particle density of state previously introduced in Eq. (14). We will consider the weak-disorder limit which is controlled by the small parameter $(E_F \tau)^{-1}$, with E_F the Fermi energy. In the diagrammatic impurity technique, the first step is the introduction of the irreducible self-energy in the self-consistent Born approximation for the electron Green function.

6.1 The case of the E^{xy} bands

The Green function, due to the SOC of the lowest pair of bands H_{xy}^{SOC} of Eq. (27), can be expanded in Pauli matrices as $G = G_0 \tau^0 + G_1 \tau^x + G_2 \tau^y$ and explicitly reads

$$G(\epsilon, \mathbf{k}) = \frac{G_+(\epsilon, \mathbf{k}) + G_-(\epsilon, \mathbf{k})}{2} \tau^0 - (\tau^x \hat{k}_y - \tau^y \hat{k}_x) \frac{G_+(\epsilon, \mathbf{k}) - G_-(\epsilon, \mathbf{k})}{2} \quad (36)$$

where

$$G_{\pm}(\epsilon, \mathbf{k}) = [\epsilon - E_{\pm}^{xy}(\mathbf{k}) - \Sigma(\epsilon)]^{-1}, \quad (37)$$

and the self-energy has the form

$$\Sigma(\epsilon) = \mp \frac{i}{2\tau} \tau^0, \quad (38)$$

the minus and plus signs applying to the retarded (R) and advanced (A) sectors, respectively. The scattering time τ entering Eq. (38) is exactly the one required by the Fermi golden rule. It is worth noticing that the self-energy is proportional to the identity matrix in the spin space.⁵⁰ Once the Green function is known, we may compute the SGC by means of the Kubo formula

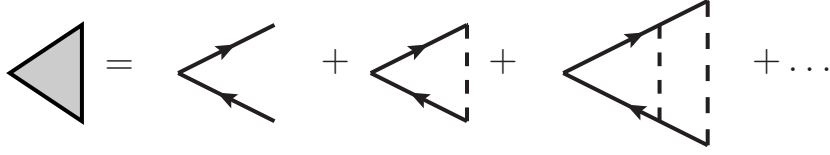


Figure 4. Ladder diagrams for the determination of the dressed vertex. The gray-filled triangle represents the infinite sum of diagrams, which results from repeated scattering. The solid lines with arrows are Green function propagators for electrons, whereas the dashed lines represent the operation of impurity average.

$$\sigma^{ISG} = \frac{1}{2\pi} \langle \text{Tr} [S^y G^R J_x G^A] \rangle_{\text{dis av}} \quad (39)$$

which can be obtained from the expression (5), after averaging over the disorder configurations, represented as $\langle \dots \rangle_{\text{dis av}}$. In the above the $\text{Tr} \dots$ symbol involves all degrees of freedom, i.e. spin and space coordinates. The disorder average in Eq. (39) enters in two ways. The first is to use the disorder-averaged Green function given in Eq. (36). The second is the introduction, to lowest order in the expansion parameter $(E_F \tau)^{-1}$, of the so-called ladder diagrams, which lead to vertex corrections. The vertex corrections procedure can be performed either for the spin or charge vertex of Eq. (39). Here we consider the vertex correction for the charge current vertex. The *dressed* vertex \tilde{J}_x obeys the Bethe–Salpeter equation

$$\tilde{J}_x = J_x + n_i u^2 \sum_{\mathbf{k}} G^R(\epsilon, \mathbf{k}) \tilde{J}_x G^A(\epsilon, \mathbf{k}), \quad (40)$$

which results from the infinite summation of ladder diagrams, as shown in Fig. 4. In terms of the dressed vertex the SGC reads

$$\sigma^{ISG} = \frac{1}{2\pi} \sum_{\mathbf{k}} \text{tr} \left[S^y G^R(\epsilon, \mathbf{k}) \tilde{J}_x G^A(\epsilon, \mathbf{k}) \right], \quad (41)$$

where now the lower case trace symbol involves the spin degrees of freedom only. The problem is then reduced to the solution of the Bethe–Salpeter equation (40) and to the evaluation of the bubble (41). In general the Bethe–Salpeter equation is an integral equation. However, in the present case of white-noise disorder, the Bethe–Salpeter equation becomes an algebraic one, even though still having a spin structure. In the appendix A we provide the details of the solution of Eq. (40), which leads to

$$\tilde{J}_x = (-e) \frac{k_x}{m}, \quad (42)$$

which shows that the vertex corrections exactly cancel the interband matrix elements of the charge current vertex. As a result, the evaluation of Eq. (41) leads to

$$\sigma_{xy}^{ISG} = e N_0 \alpha_{xy} \tau, \quad (43)$$

which must be compared with the Drude weight evaluated in Eq. (31).

6.2 The case of the E^- bands

According to the analysis of appendix A, the dressed charge current vertex reads

$$\tilde{J}_x = (-e) \left[\frac{k_x}{m} \tau^0 - 2\beta k_x k_y \tau^x + \beta(3k_x^2 - k_y^2) \tau^y + \frac{1}{4} \beta p_F^2 \tau^y \right].$$

The evaluation then of Eq. (41) leads to

$$\sigma_-^{ISG} = -\frac{5}{8}eN_0\gamma\beta p_F^4\tau, \quad (44)$$

which has a sign opposite to that of the E^{xy} bands. In Eq. (44) the combination βp_F^2 plays the role of an effective SOC, whereas γp_F^2 is the spin dressing factor accounting for the interactions in the original model.

6.3 The case of the E^+ bands

According to the analysis of appendix A, the dressed charge current vertex reads

$$\tilde{\mathbf{J}}_x = (-e)\frac{k_x}{m}\tau^0.$$

The evaluation then of Eq. (41) leads to

$$\sigma_+^{ISG} = (\gamma p_F^2)eN_0\alpha_+\tau, \quad (45)$$

which shows again a change of sign with respect to that of the E^- bands. Also here the combination γp_F^2 is the spin dressing factor accounting for the interactions in the original model.

7. THE NUMERICAL APPROACH

In this section we present our numerical results. The starting point is the response function defined in Eq. (5), which may be expressed as follows

$$R_{yx}(\omega) = \frac{1}{N} \sum_{k,p} (f_p - f_k) \frac{\langle p|S^y|k\rangle \langle k|J_x|p\rangle}{\omega + i\eta + E_p - E_k}, \quad (46)$$

where k and p are quantum numbers labelling the eigenstates of the Hamiltonian. For instance, in the absence of disorder, the index k includes the crystal momentum, the orbital and spin degrees of freedom. The symbol f_k stands for the Fermi function evaluated at the energy of the eigenstate k . In Eq. (46) N is the number of lattice sites. The numerical evaluation is performed on a finite system and then it is convenient to separate from the outset the Drude singular weight from the regular part as follows

$$D^{ISG} = -\frac{\pi}{N} \sum_{k,p} \frac{f_p - f_k}{E_p - E_k} \Re \langle p|S^y|k\rangle \langle k|J_x|p\rangle, \quad (47)$$

$$\sigma_{reg}^{ISG} = \lim_{\omega \rightarrow 0} \mathcal{P} \frac{R_{yx}''(\omega)}{\omega} = -\frac{1}{N} \sum_{k,p} \frac{f_p - f_k}{E_p - E_k} \Im \frac{\langle p|S^y|k\rangle \langle k|J_x|p\rangle}{i\eta + E_p - E_k}, \quad (48)$$

where \Re and \Im indicate the real and imaginary parts.

Fig. 5 shows the behavior of the spin-orbit split gap at the Fermi surface. Inspection of Fig. 5 reveals that for $\mu = 0.3$ eV the gap has extrema at energies $\Delta \approx 0.005$ and 0.009 eV which are expected to dominate the response due to the ‘‘saddle-point’’ character of the corresponding states as discussed below. For $\mu = 0.7$, as shown in Fig. 2, all bands are occupied and all the gaps will appear in the response function. In particular the pair of bands (1,2) contributes to the gap at energies $\Delta \approx 0.015$ eV, the pair of bands (3,4) at energies $\Delta \approx 0.005 - 0.015$ eV, and the pair of bands (5,6) at energies $\Delta \approx 0$.

Fig. 6 shows the frequency dependence of the real and imaginary parts of the response function $R_{yx}(\omega)$ for the three chemical potentials $\mu = 0.3$ eV, $\mu = 0.425$ eV and $\mu = 0.7$ eV. The underlying ground state is for a homogeneous system but we investigate the influence of the particle-hole lifetime parameter η . As compared with the approach discussed in Sec. 6 this mimics the inclusion of momentum relaxation without considering vertex corrections. For $\mu = 0.3$ eV, when only the lowest pair of bands is occupied, one may interpret the observed behavior in terms of the Rashba model of Eq. (9). The low energy structure is determined by transitions across

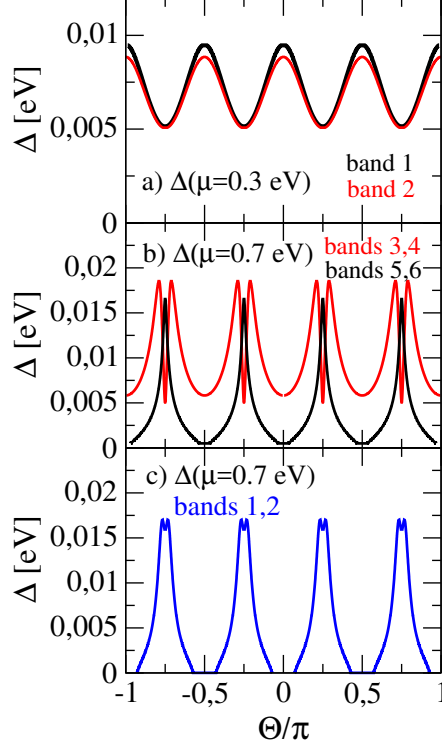


Figure 5. Size of the spin-orbit split gap around the Fermi surface for $\mu = 0.3$ eV (a) and $\mu = 0.7$ eV (b,c). This is obtained by determining the cut k_F of each band with μ and then calculating the energy difference to the 'other' SO split band at the same k_F . If the SO interaction has some significant momentum dependence around k_F the gap determined for each of the two bands from a pair may slightly differ as in panel (a). The angle Θ is defined with respect to the k_x -axis.

the spin-orbit split gap of the same t_{2g} band. In fact, it is exactly in this energy range that the imaginary part of $R_{yx}(\omega)$ develops a peak structure as discussed in Eq.(13). In the clean system, i.e. lifetime parameter $\eta \rightarrow 0$, the imaginary part vanishes for energies below the minimum gap excitations and therefore the slope of $R''_{yx}(\omega)$, which determines the regular ISG response $\sigma_{yx,reg}^{ISG}$, is zero, whereas the limiting value of the real part fixes the Drude weight of the singular contribution. As shown in Fig. 6 (panel (a)) a finite η (or, similarly, a finite temperature) broadens the excitations and therefore induces a finite slope of $R''_{yx}(\omega)$ at $\omega = 0$ leading thus to a finite ISG response. This is evidenced by making η larger in Fig. 6: the red curve is for $\eta = 10^{-5}$, while the blue one for $\eta = 10^{-3}$. The fact, that the ISG response vanishes for a clean system is consistent with the analysis in Ref. ⁴¹ and with the discussion at the end of section 3. According to the KKR (7), the sign of the imaginary part of the ISG response function is determined by the sign of the effective Rashba SOC. The negative sign shown by the numerical evaluation of Fig. 6 agrees with the sign found for the coupling $-\alpha_{xy}$ in the effective model for the lowest pair of xy bands in Eq. (31). We remind that the Drude weight is determined by the zero-frequency value of the real part, which is obtained from the imaginary part via the KKR (7).

For the chemical potential $\mu = 0.425$ eV, close to the Lifshitz point, all the bands are occupied and the imaginary part of the response function gets contributions from the interband transitions across the spin-orbit split gaps of all the pairs of bands as well as from the interband transitions involving different pairs of bands simultaneously. In panel (b) of Fig. 6 this is evidenced by showing, together with the full imaginary part (red line) also the contribution of the individual pairs of bands: (1,2) (green line), (3,4) (blue dashed line) and (5,6) (yellow line). From this we conclude that the large spectral weight at energy $\omega = 0.02$ is due to interband transition between different pairs of bands. The green curve shows that the contribution due exclusively to the lowest pair of bands (1,2) is still around the same energy as in panel (a) and hence the behavior of this pair of bands is still

well described by the effective Rashba model of Eq.(27). On the other hand, the inset around zero energy in panel (b) shows how the low energy contribution is dominated by both the pairs of bands (3,4) and (5,6), which at this chemical potential have a small Fermi surface and a small spin-orbit split gap. Notice that the sign of the imaginary part is opposite to that of bands (1,2), indicating an opposite sign for the Drude spectral weight in the limit of vanishing lifetime parameter η in agreement with Eqs.(33) and (35). Furthermore one may notice that for the small but finite value used for the lifetime parameter η both pairs of bands yield a finite positive slope at zero frequency. Whereas the regular part at zero frequency has the sign due to the pair or pairs of bands with the lowest gap, the zero-frequency value of the real part, which is associated to the Drude spectral weight, is obtained from the integrated spectral weight of all the interband transitions. As a consequence, also interband transitions at high energy may contribute provided they have a strong spectral weight, which must compensate the big frequency denominator of the KKR relation (7). As it is apparent from panel (b), close to the Lifshitz point, the very small value of the gap of the pairs of bands (3,4) and (5,6) is sufficient to determine a positive value of the zero-frequency real part.

For the chemical potential $\mu = 0.7$ eV as well, the energy response is determined by the gap structure of all the bands (1,2), (3,4) and (5,6), as is evident from Fig. 2, even though now we are far away from the Lifshitz point. As shown in panel (c) of Fig. 6 and the inset at zero frequency, the peak coming from the smallest gap excitations at $\omega \approx 0.0001$ eV belongs to the pair of bands (5,6) with the smaller k_F . The next higher excitation comes from the pair of bands (3,4). As a result at a finite value of the lifetime parameter, the regular part of the ISG response is finite and positive. However, in this case, in contrast to what happens close to the Lifshitz point, the opposite-in-sign spectral weight of the interband transitions at higher energies is sufficiently strong to drive the sign of the real part to a negative value.

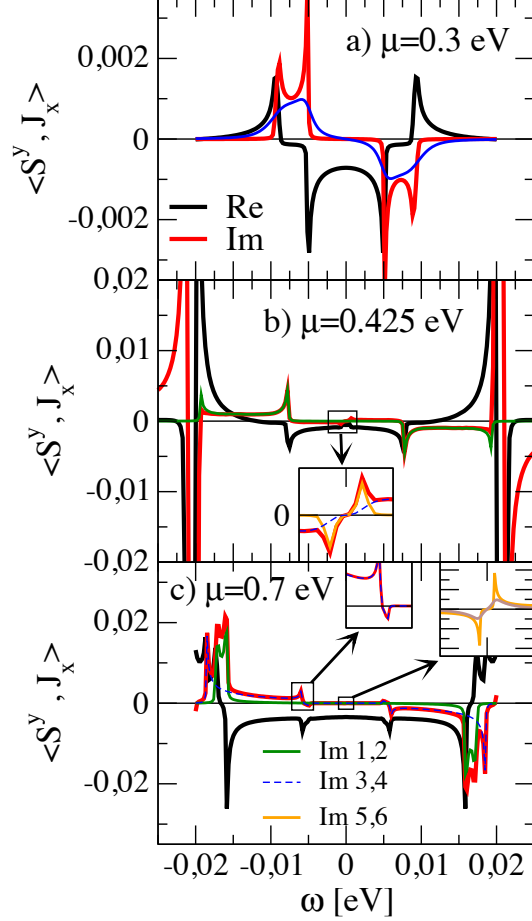


Figure 6. Frequency dependent real (black line) and imaginary part (red line) of the spin-current correlation function $R_{yx}(\omega)$ evaluated for chemical potentials $\mu = 0.3 \text{ eV}$ (a), $\mu = 0.425 \text{ eV}$ (b) and $\mu = 0.7 \text{ eV}$ (c) and lifetime parameter $\eta = 5 \cdot 10^{-5} \text{ eV}$. In panel (a), the additional blue line is for $\eta = 10^{-3} \text{ eV}$ and the slope of the imaginary part at $\omega = 0$ defines the SGC σ_{reg}^{ISG} . In panel (b), the individual contribution of the pair of bands (1,2) (green line), (3,4) (blue dashed line) and (5,6) (yellow line) is also shown. The inset details the behavior around $\omega = 0$, dominated by the pairs of bands (3,4) and (5,6). In panel (c) the individual contribution of the different pairs of bands is shown as in panel (b). The inset around $\omega = 0$ evidences the contribution from the pair (5,6) at two different values of the lifetime parameter $\eta = 10^{-4}$ (brown line) and $\eta = 10^{-5}$ (yellow line), whereas the inset around $\omega = 0.075$ shows the contribution from the pair of bands (3,4) at $\eta = 10^{-4}$ (blue dashed line) and $\eta = 10^{-5}$ (magenta line).

The analysis carried out in Fig. 6 can be extended to all values of the chemical potential and the result is reported in Fig. 7. Panel (a) of Fig. 7 shows the full Drude spectral weight together with the contribution of the individual pairs of bands at $T = 10 \text{ K}$ as a function of the chemical potential. The Drude part, which is associated to the integrated imaginary part of the response, does not depend significantly on the temperature and on the lifetime parameter η (Fig. 7 is for $\eta = 1 \cdot 10^{-6}$). Close to the Γ points of all the bands one finds a negative Drude coefficient for the pair of bands (1,2) and a positive coefficient for the pairs of bands (3,4) and (5,6). This is in agreement with results of the effective model discussed in section 4.

Panel (b) of Fig. 7 reports on the other hand the regular part of the ISG response as function of the chemical potential. For small lifetime parameter $\eta = 1 \cdot 10^{-6}$ (inset) the response is only significant around the energies where the DOS displays a van-Hove singularity. In particular, the response at low chemical potentials is suppressed because there the spin-orbit split gap is large and $\eta = 1 \cdot 10^{-6}$ is not sufficient to broaden the excitations up to $\omega = 0$. On the other hand, for $\eta = 1 \cdot 10^{-4}$ (main panel) one now observes a ISG response at all energies

and also the sign change upon crossing around the Lifshitz point as discussed for panel (b) of Fig. 6. Such a sign change has been also found in the experiment of Ref.²⁶

It can also be seen that the total ISG regular response is given by the sum of the three contributions coming from the interband transitions between each of the three pairs of the spin-orbit split bands. In fact, we have seen that a finite σ^{ISG} requires a broadening of the same order than the energy of the contributing low energy excitation. Therefore interband transitions between different pairs of bands cannot contribute due to their high excitation energies.

Since we investigate a clean system, we also obtain a finite value for the Drude part D^{ISG} which we checked not to depend on the system size but is a robust result. In the presence of (real) disorder we expect $D^{ISG} = 0$ which then guarantees the stationarity of the solution.

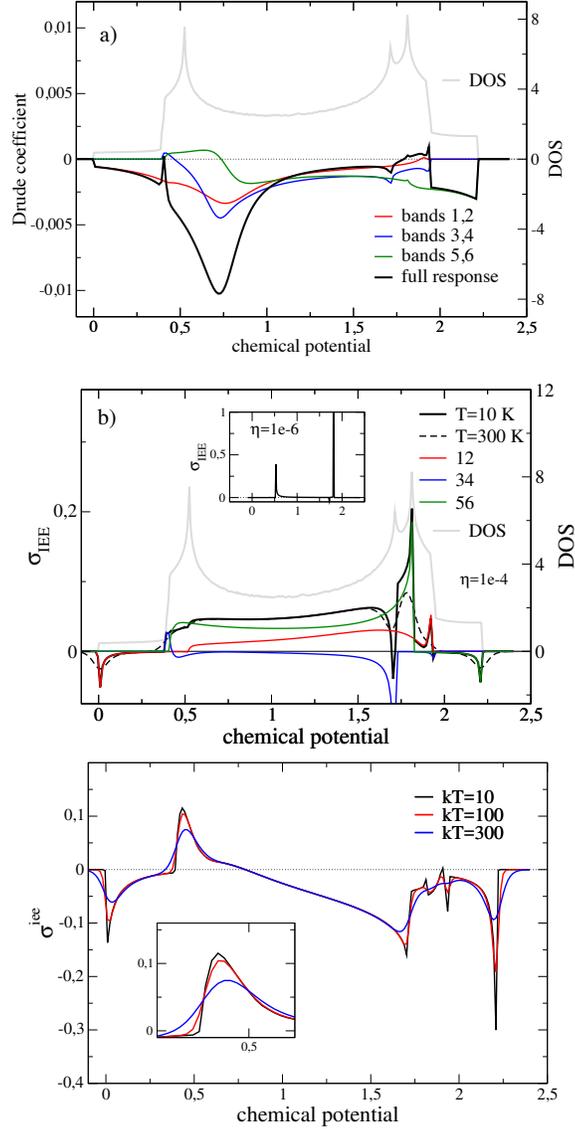


Figure 7. Top panel: Drude coefficient at $T = 10$ K (black) of the ISG response and the contribution of the individual bands. Middle panel: Regular part of the inverse ISG response as a function of chemical potential for lifetime parameter $\eta = 1 \cdot 10^{-4}$ and the contribution of the individual bands. In both panels the DOS is shown in grey for comparison. The inset to the middle panel reports the regular part for $\eta = 1 \cdot 10^{-6}$ and $T = 10$. Lowest panel: Regular part for $\eta = 1 \cdot 10^{-3}$ and different temperatures. The inset to the lowest panel resolves the region around the Lifshitz point with a significant temperature dependence. Calculations have been done for a lattice with 6354×6354 k points.

To implement the effect of disorder scattering we perform the calculation of the SGC on finite lattices. In order to reduce the finite size effects we average over twisted boundary conditions, i.e. for a $L_x \times L_y$ lattice we set

$$|\Psi(R_i)\rangle = e^{i\Phi_{x,y}} |\Psi(R_i + L_{x,y})\rangle$$

with $\Phi_{x,y} \in [0, 2\pi]$ and we typically average over 50 randomly chosen (Φ_x, Φ_y) . The inset to Fig. 8 demonstrates that the averaged finite lattice computation reproduces the doping dependent SGC of the 'infinite' lattice calculation.

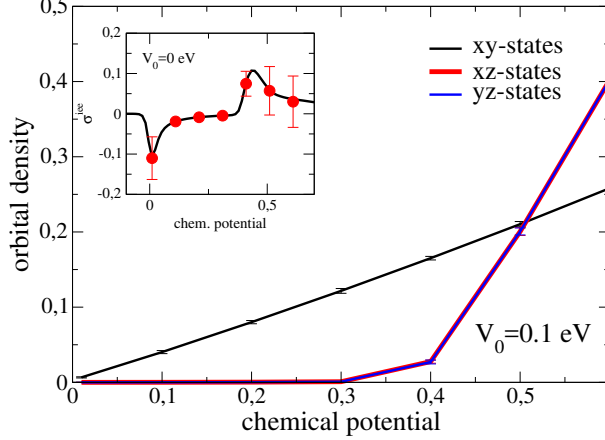


Figure 8. Inset: Comparison of the ISG response for a homogeneous ($V_0 = 0$) 24×24 lattice (red symbols) with the calculation for a 3762×3762 lattice (black line). Main panel: Averaged orbital occupation as a function of chemical potential for a 24×24 lattice and disorder potential $V_0 = 0.1$ eV. Further parameters: temperature $T = 100$ K, $\eta = 1 \cdot 10^{-3}$ eV.

Disorder is introduced by a random local potential

$$\hat{V} = \sum_{i,\sigma} V_i (|xy_{i,\sigma}\rangle\langle xy_{i,\sigma}| + |xz_{i,\sigma}\rangle\langle xz_{i,\sigma}| + |yz_{i,\sigma}\rangle\langle yz_{i,\sigma}|)$$

with V_i randomly chosen on each site in the interval $[-V_0, +V_0]$. We then compute the SGC at some specified values of the chemical potential and average over phases $\Phi_{x,y}$ and the disorder configurations. The main panel of Fig. 8 demonstrates that for $V_0 = 0.1$ eV the averaged orbital occupations are still well defined for a given value of the chemical potential.

According to the analytical results of section 6, in the presence of disorder, the SGC is positive for the pair of bands (1,2) due to the d_{xy} orbitals (cf. Eq.(43)), is negative for the pair of bands (3,4) (cf. Eq.(44)), associated to the effective model of bands E^- , finally is positive again for the pair of bands (5,6) (cf. Eq.(45)), associated with bands E^+ . One then would expect a double change of sign as the chemical potential enters the bottom of the different pairs of bands. The numerical analysis of the clean limit with inclusion of the effect of all the bands has shown a more complex behavior. Close to the Γ point, the behavior of the regular SG response at zero frequency of the individual bands is well described by the effective model. Instead, the Drude weight, which also includes all interband transitions, cannot be simply interpreted in terms of the individual contributions of the different pairs of bands.

Fig. 9 shows the SGC of the disordered system for four different temperatures, obtained by averaging over 50 disorder configurations and over 100 phase pairs (Φ_x, Φ_y) for each disorder realization. To estimate the effective strength of the disorder, we have evaluated the frequency-dependent electrical longitudinal conductivity, whose Lorentzian lineshape allows to extract the elastic scattering time τ , used in the analytical theory of section 6. For two chemical potentials $\mu = 0.2$ eV and $\mu = 0.6$ eV, below and above the Lifshitz point, the estimated scattering time is of the order of 10^{-2} ps, which corresponds to a level broadening of the order of 10^{-5} eV. In the presence of the SOC a crucial parameter is the ratio between the spin-orbit split gap and the disorder-induced broadening. Keeping in mind the typical size of the spin-orbit split gap shown in Fig. 5, one may conclude that the condition of weak scattering limit is satisfied. At zero temperature, the black line in Fig. 9 shows that the SGC changes sign twice. One sees that the two sign changes occur in a very restricted range of chemical potentials, when first the pair of bands (3,4) starts to be occupied and then also the pair of bands (5,6) becomes occupied as well. One then is tempted to associate the positive sign with the initial filling of bands (3,4) and the negative sign with the filling of bands (5,6) in agreement with the analytical results of Eqs.(44) and (45). The effect of the temperature reduces the value of the SGC. This happens when the energy scale associated with the temperature becomes larger than disorder broadening, which is the situation already at 100 K. At finite

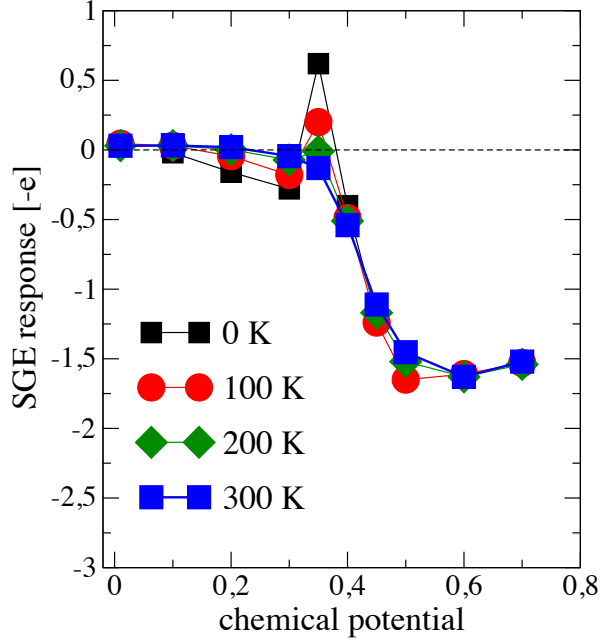


Figure 9. Regular part of the SGC response as a function of chemical potential. Disorder potential is $V_0 = 0.1$ eV and calculations are performed on 24×24 lattices.

temperature the SGC is likely to be an effective average over its value at different chemical potentials, and hence over the values associated to the different pairs of bands. As a result, at the highest temperature 300 K, there is only one sign change before the Lifshitz point. Previously⁴² it has been noticed that the behavior at $T = 300$ K is compatible with the experimental behavior of Ref.,²⁸ whereas the sign change upon voltage reversal of the experiment of Ref.,²⁶ performed at $T = 7$ K, can be interpreted as the second sign change of our $T = 0$ K curve.

8. CONCLUSIONS

In this paper we have presented a detailed theoretical investigation of the spin galvanic effect in a multi-band model describing the electron states at a LAO/STO metallic interface. Starting from a tight-binding description, we have derived a low-energy continuum model, which well describes the original model close to the Γ point. The resulting effective Rashba-like models correspond to a linear-in-momentum SOC for the lowest and highest pair of bands while it is cubic for the middle pair of bands. For these effective models we have performed analytical calculations both in the absence and in the presence of disorder. In particular, we have used the standard diagrammatic approach of impurity technique valid in the metallic regime. We have also performed exact numerical calculations, which are in agreement with the analytical ones close to the Γ point. The main results can be summarized as follows. 1) In the absence of disorder, the SGC as a function of frequency of the driving electric field has a singular delta-like behavior reminiscent of the Drude peak in the standard optical electrical conductivity. The spectral strength associated to the delta function gets contributions from all the interband transitions and, in general, cannot simply be attributed to a single pair of spin-orbit split bands. 2) The frequency-dependent SGC has also a regular contribution, which in the absence of disorder vanishes exactly at zero frequency. This regular part has a number of spectral features, whose associated frequencies correspond to the possible interband transitions. 3) A generic level-broadening mechanism leads to a finite regular part at low frequency, whose behavior is then dominated by the smallest energy interband transition. The latter then can be directly linked to a specific pair of spin-orbit split bands. A numerical calculation inevitably requires a finite level broadening and we have shown the effect of varying the size of the broadening. 4) The presence of disorder guarantees a stationary solution and introduces an intrinsic level broadening, whose effective strength we have estimated by looking at the Lorentzian lineshape of the electrical conductivity as function of frequency.

Note that in contrast to the SGC, the spin Hall effect for a Rashba model with linear coupling (as for the lowest xy-type bands) would vanish⁴⁸ under stationary conditions and can only be sustained under special conditions, as e.g. a periodic modulation of the chemical potential.⁴⁹ 5) The behavior of the SGC as a function of the chemical potential shows a non monotonous behavior at zero temperature, which evolves to a monotonous one when the temperature becomes larger than the level broadening. 6) Our theoretical results are compatible with recent experiments and call for a systematic study of the voltage dependence as a function of the temperature.

ACKNOWLEDGMENTS

G. S. acknowledges support from the Deutsche Forschungsgemeinschaft under SE806/19-1. S. C. acknowledge financial support from the University of Rome Sapienza Research Project No. RM116154AA0AB1F5.

APPENDIX A. THE BETHE–SALPETER EQUATION FOR THE CHARGE CURRENT VERTEX

In this appendix we provide a few details on the solution of the Bethe–Salpeter equation for the vertex. We follow closely the discussion developed for the case of the Rashba 2DEG model.⁵⁰

A.1 The case of the E^{xy} bands

We begin with the case of the lowest pair of bands due to the d_{xy} orbitals. This case is practically equivalent to the standard Rashba 2DEG model. Since vertex corrections do not modify the momentum dependence of the vertex, it is useful to write the full vertex as

$$\tilde{J}_x = (-e) \frac{k_x}{m} \tau^0 + \Gamma_x, \quad (49)$$

where all the momentum dependence is limited to the *bare* vertex $(-e)k_x/m$. The spin-dependent part of the vertex Γ_x satisfies then a new Bethe–Salpeter equation

$$\Gamma_x = \gamma_x + n_i u^2 \sum_{\mathbf{k}} G^R \Gamma_x G^A, \quad (50)$$

where the effective bare vertex is defined by

$$\gamma_x = (-e) \alpha_{xy} \tau^y + n_i u^2 \sum_{\mathbf{k}} G^R (-e) \frac{k_x}{m} G^A. \quad (51)$$

In the above we have omitted for the sake of simplicity the explicit frequency and momentum dependence of the Green functions. To evaluate the integral over the momentum, one must use the Pauli matrix expansion of the Green function shown in Eq. (36). Because of the factor k_x in the integral, only the combination $G_0^R G_2^A$ and its complex conjugate appear. As a result the integral in the right hand side of Eq. (51) is proportional to τ^y and exactly cancels the first term so that the vertex γ_x vanishes (see Ref.⁴⁸ for details) and the full vertex reduces to the standard current vertex as shown in Eq. (42).

A.2 The case of the E^- bands

We follow the same strategy as in the previous case. The Green function has now the form (we omit the frequency and momentum dependence for brevity)

$$\hat{G} = \frac{G_+ + G_-}{2} - \frac{\zeta}{|\zeta|} (\tau^x \hat{k}_y - \tau^y \hat{k}_x) \frac{G_+ - G_-}{2}, \quad (52)$$

where ζ was introduced in Eq. (32). In this case the effective bare vertex reads

$$\gamma_x = (-e) n_i u^2 \sum_{\mathbf{k}} G^R \left(\frac{k_x}{m} \tau^0 - 2\beta k_x k_y \tau^x + \beta(3k_x^2 - k_y^2) \tau^y \right) G^A = (-e) \frac{1}{4} \beta p_F^2 \tau^y, \quad (53)$$

which must be inserted in Eq. (50) with the form of the Green functions given by Eq. (52). In the above p_F is the Fermi momentum in the absence of SOC. Given the form (53), we look for a solution of the form $\Gamma_x = \Gamma_x^y \tau^y$. With this ansatz, one easily sees that the integral over the momentum in Eq. (50) yields a term proportional to τ^y . As a result one has the closed equation

$$\Gamma_x^y = \gamma_x^y + I \Gamma_x^y = \frac{\gamma_x^y}{1 - I}, \quad (54)$$

where

$$I = n_i u^2 \sum_{\mathbf{k}} \frac{1}{2} \text{Tr} [\tau^y G^R \tau^y G^A] = 1 - \frac{1}{2} \left\langle \frac{4\beta^2 p_F^6 \zeta^2 \tau^2}{1 + 4\beta^2 p_F^6 \zeta^2 \tau^2} \right\rangle, \quad (55)$$

where $\langle \dots \rangle$ stands for the angle average over the direction of momentum. In the weak disorder limit, $\tau \rightarrow \infty$, $I = 1/2$. As a result $\Gamma_x^y = (-e)\beta p_F^2/2$.

A.3 The case of the E^+ bands

In this case the Green function reads

$$\hat{G} = \frac{G_+ + G_-}{2} + (\tau^x \hat{k}_y + \tau^y \hat{k}_x) \frac{G_+ - G_-}{2}. \quad (56)$$

The evaluation of the effective bare vertex is similar to the case of the E^{xy} bands with the replacement $\alpha_{xy} \rightarrow \alpha_+$. As a result $\gamma_x = 0$ and the dressed vertex coincides with the momentum dependent part of the bare vertex.

APPENDIX B. THE BETHE–SALPETER EQUATION AT FINITE FREQUENCY

For the Rashba 2DEG model (9), the Bethe–Salpeter equation at finite frequency reads

$$\Gamma_x = \gamma_x + n_i u^2 \sum_{\mathbf{k}} \frac{1}{2} \text{Tr} \left\{ \tau^y G_{\mathbf{k}}^R(\omega/2) \tau^y \Gamma_x G_{\mathbf{k}}^A(-\omega/2) \right\} \quad (57)$$

$$\gamma_x = e\alpha\tau^y + n_i u^2 \sum_{\mathbf{k}} \frac{1}{2} \text{Tr} \left\{ \tau^y G_{\mathbf{k}}^R(\omega/2) (-e) \frac{k_x}{m} G_{\mathbf{k}}^A(-\omega/2) \right\}. \quad (58)$$

which has the solution

$$\Gamma_x = -e \frac{\gamma_x}{\tau/\tau_s - i\omega\tau}, \quad \gamma_x = (-e)\alpha \frac{i\omega}{-i\omega + 1/\tau} \tau^y.$$

The dressed vertex reads then

$$\tilde{J}_x = (-e) \frac{k_x}{m} \tau^0 + -e \frac{1}{\tau/\tau_s - i\omega\tau} \alpha \frac{i\omega}{-i\omega + 1/\tau} \tau^y. \quad (59)$$

When the full dressed vertex (59) is used in the Kubo formula (39) one obtains Eq. (18).

REFERENCES

- [1] E. I. Rashba, *Fiz. Tverd. Tela* **2**, 1224 (1960) [*Sov. Phys. Solid State* **2**, 1109 (1960)] [1](#)
- [2] [1] Yu. A. Bychkov and E. I. Rashba, *Sov. Phys. - JETP Lett.* **39**, 78 (1984). [1](#)
- [3] Yu. A. Bychkov and E. I. Rashba, *J Phys C: Solid State Phys.* **17**, 6039 (1984). [1](#), [3](#)
- [4] S. D. Ganichev, M. Trushin, and J. Schliemann, Spin orientation by electric current, in *Handbook of Spin Transport and Magnetism*, edited by E. Y. Tsymbal and I. Zutic (Chapman and Hall, Boca Raton, FL, 2016), second edition, extended. [1](#)
- [5] M. I. Dyakonov and V. I. Perel, *Phys. Lett. A* **35**, 459 (1971). [1](#)
- [6] E. L. Ivchenko and G. E. Pikus, *JETP Lett.* **27**, 604 (1978). [1](#)
- [7] L. E. Vorob'ev, E. L. Ivchenko, G. E. Pikus, I. I. Farbshten, V. A. Shalygin, and A. V. Shturbin, *JETP Lett.* **29**, 441 (1979). [1](#)
- [8] V. M. Edelstein, *Solid State Communications* **73**, 233 (1990). [1](#), [3](#), [6](#)
- [9] E. L. Ivchenko, Y. B. Lyanda-Geller, and G. E. Pikus, *JETP Lett.* **50**, 175 (1989). [1](#)
- [10] A. G. Aronov and Y. B. Lyanda-Geller, *JETP Lett.* **50**, 431 (1989). [1](#)
- [11] L. Levitov, Y. V. Nazarov, and G. Eliashberg, *Sov. Phys. JETP* **61**, 133 (1985). [1](#)
- [12] S. D. Ganichev, E. L. Ivchenko, S. N. Danilov, J. Eroms, W. Wegscheider, D. Weiss, and W. Prettl, *Phys. Rev. Lett.* **86**, 4358 (2001). [1](#)
- [13] S. D. Ganichev, E. L. Ivchenko, V. V. Belkov, S. A. Tarasenko, M. Sollinger, D. Weiss, W. Wegscheider, and W. Prettl, *Nature (London)* **417**, 153 (2002) [1](#)
- [14] Y. K. Kato, R. C. Myers, A. C. Gossard, and D. D. Awschalom, *Phys. Rev. Lett.* **93**, 176601 (2004). [1](#)
- [15] Y. K. Kato, R. C. Myers, A. C. Gossard, and D. D. Awschalom, *Science* **306**, 1910 (2004). [1](#)
- [16] V. Sih, R. C. Myers, Y. K. Kato, W. H. Lau, A. C. Gossard, and D. D. Awschalom, *Nat. Phys.* **1**, 31 (2005). [1](#)
- [17] C. L. Yang, H. T. He, L. Ding, L. J. Cui, Y. P. Zeng, J. N. Wang, and W. K. Ge, *Phys. Rev. Lett.* **96**, 186605 (2006). [1](#)
- [18] H. J. Chang, T. W. Chen, J. W. Chen, W. C. Hong, W. C. Tsai, Y. F. Chen, and G. Y. Guo, *Phys. Rev. Lett.* **98**, 136403 (2007). [1](#)
- [19] B. M. Norman, C. J. Trowbridge, D. D. Awschalom, and V. Sih, *Phys. Rev. Lett.* **112**, 056601 (2014). [1](#)
- [20] M. Luengo-Kovac, S. Huang, D. Del Gaudio, J. Occena, R. S. Goldman, R. Raimondi, V. Sih *Phys. Rev. B* **96**, 195206 (2017). [1](#)
- [21] J. C. R. Sánchez, L. Vila, G. Desfonds, S. Gambarelli, J. P. Attané, J. M. D. Teresa, C. Magén, and A. Fert, *Nat. Commun.* **4**, 2944 (2013). [1](#)
- [22] L. Chen, M. Decker, M. Kronseder, R. Islinger, M. Gmitra, D. Schuh, D. Bougeard, J. Fabian, D. Weiss, and C. H. Back, *Nat. Commun.* **7**, 13802 (2016).
- [23] A. R. Mellnik, J. S. Lee, A. Richardella, J. L. Grab, P. J. Mintun, M. H. Fischer, A. Vaezi, A. Manchon, E.-A. Kim, N. Samarth et al., *Nature (London)* **511**, 449 (2014). [1](#)
- [24] Y. Shiomi, K. Nomura, Y. Kajiwara, K. Eto, M. Novak, K. Segawa, Y. Ando, and E. Saitoh, *Phys. Rev. Lett.* **113**, 196601 (2014). [1](#)
- [25] J.-Y. Chauleau, M. Boselli, S. Gariglio, R. Weil, G. de Loubens, J.-M. Triscone, and M. Viret, *Europhys. Lett.* **116**, 17006 (2016). [1](#)
- [26] E. Lesne, S. O. Y. Fu, J. C. Rojas-Sánchez, D. C. Vaz, H. Naganuma, G. Sicoli, J.-P. Attané, M. Jamet, E. Jacquet, J.-M. George et al., *Nat. Mater.* **15**, 1261 (2016). [1](#), [7](#), [7](#)
- [27] Y. Wang, R. Ramaswamy, M. Motapohtula, K. Narayanapillai, D. Zhu, J. Yu, T. Venkatesan, and H. Yang, *Nano Lett.* **17**, 7659 (2017). [1](#)
- [28] Q. Song, H. Zhang, T. Su, W. Yuan, Y. Chen, W. Xing, J. Shi, J. Sun, and W. Han, *Sci. Adv.* **3**, e1602312 (2017). [1](#), [7](#)
- [29] S. Caprara, *Nat. Materials* **15**, 1124 (2016). [1](#)
- [30] Y. Ando and M. Shiraishi, *J. Phys. Soc. Jpn.* **86**, 011001 (2017). [1](#)
- [31] A. Soumyanarayanan, N. Reyren, A. Fert, and C. Panagopoulos, *Nature (London)* **539**, 509 (2016). [1](#)
- [32] J. Varignon, L. Vila, A. Barthélémy and M. Bibes, *Nat. Physics* **14**, 322 (2018). [1](#)

- [33] Wei Han, Y. Otani and S. Maekawa, *Quantum Materials* **3**, 27 (2018). [1](#)
- [34] A. D. Caviglia, M. Gabay, S. Gariglio, N. Reyren, C. Cancellieri, and J.-M. Triscone *Phys. Rev. Lett.* **104**, 126803 (2010). [1](#)
- [35] S. Hurand, A. Jouan, C. Feuillet-Palma, G. Singh, J. Biscaras, E. Lesne, N. Reyren, A. Barthélémy, M. Bibes, J. E. Villegas, C. Ulysse, X. Lafosse, M. Pannetier-Lecoecur, S. Caprara, M. Grilli, J. Lesueur and N. Bergeal, *Sci. Rep.* **5**, 12751 (2015). [1](#)
- [36] K. Gopinadhan, A. Annadi, Y. Kim, A. Srivastava, B. Kumar J. Chen, J. M. D. Coey, Araindo, T. Venkatesan, *Adv. Mater.* **3**, 1500114 (2015). [1](#)
- [37] Haixing Liang, Long Cheng, Laiming Wei, Zhenlin Luo, Guolin Yu, Changgan Zeng, and Zhenyu Zhang, *Phys. Rev. B* **92**, 075309 (2015). [1](#)
- [38] Shanavas, K. V., Popović, Z. S. and Satpathy, S. *Phys. Rev. B* **90**, 165108 (2014). [1](#)
- [39] Z. Zhong, A. Tóth, and K. Held, *Phys. Rev. B* **87**, 161102 (2013). [1](#), [2](#), [2](#)
- [40] Bucheli, D., Grilli, M., Peronaci, F., Seibold, G. & Caprara, S. *Phys. Rev. B* **89**, 195448 (2014). [1](#)
- [41] K. Shen, G. Vignale, and R. Raimondi, *Phys. Rev. Lett.* **112**, 096601 (2014). [1](#), [3](#), [7](#)
- [42] G. Seibold, S. Caprara, M. Grilli, R. Raimondi, *Phys. Rev. Lett.* **119**, 256801 (2017). [1](#), [7](#)
- [43] C. Şahin, G. Vignale, and M. E. Flatté, arXiv:1804.00061. [1](#)
- [44] G. Khalsa, B. Lee, and A. H. MacDonald, *Phys. Rev. B* **88**, 041302 (2013). [2](#), [2](#)
- [45] Y. Kim, R. M. Lutchyn, and C. Nayak, *Phys. Rev. B* **87**, 245121 (2013). [2](#)
- [46] N. Scopigno, D. Bucheli, S. Caprara, J. Biscaras, N. Bergeal, J. Lesueur, and M. Grilli, *Phys. Rev. Lett.* **116**, 026804 (2016). [2](#)
- [47] R. Raimondi, M. Leadbeater, P. Schwab, E. Caroti and C. Castellani, *Phys. Rev. B* **64**, 235110 (2001). [6](#)
- [48] R. Raimondi and P. Schwab, *Phys. Rev. B* **71**, 033311 (2005). [6](#), [8](#), [A.1](#)
- [49] G. Seibold, S. Caprara, M. Grilli, R. Raimondi, *EPL* **112**, 1286 (2015). [8](#)
- [50] P. Schwab and R. Raimondi, *European Physical Journal B* **25**, 483-495 (2002). [6](#), [6.1](#), [A](#)
- [51] R. Raimondi, C. Gorini, P. Schwab, and M. Dzierzawa, *Phys. Rev. B* **74**, 035340 (2006). [3](#), [3](#)
- [52] R. Raimondi, P. Schwab, C. Gorini, and G. Vignale, *Ann. Phys. (Berlin)* **524**, 153 (2012).